Atmospheric Environment 295 (2023) 119518

Contents lists available at ScienceDirect

Atmospheric Environment

journal homepage: www.elsevier.com/locate/atmosenv

Sulfate and nitrate elevation in reverse-transport dust plumes over coastal areas of China

Wenshuai Li [a,b], Yuxuan Qi [a,b], Wen Qu [c], Wenjun Qu [a,b], Jinhui Shi [d], Daizhou Zhang [e], Yingchen Liu [a,b], Feng Wu [f], Yuanyuan Ma [a,b], Yanjing Zhang [a,b], Danyang Ren [a,b], Xueqing Du [a,b], Shishi Yang [a,b], Xinfeng Wang [g], Li Yi [a,b], Xiaomei Gao [h], Wencai Wang [a,b], Yingge Ma [i], Lifang Sheng [a,b,**], Yang Zhou [a,b,*]

[a] Frontier Science Center for Deep Ocean Multispheres and Earth System (FDOMES) and Physical Oceanography Laboratory, Ocean University of China, Qingdao, Shandong, China
[b] College of Oceanic and Atmospheric Sciences, Ocean University of China, Qingdao, Shandong, China
[c] North China Sea Marine Forecasting Center of State Ocean Administration, Qingdao, Shandong, China
[d] College of Environmental Science and Engineering, Ocean University of China, Qingdao, Shandong, China
[e] Faculty of Environmental and Symbiotic Sciences, Prefectural University of Kumamoto, Kumamoto, 862-8502, Japan
[f] Key Laboratory of Aerosol Chemistry & Physics and State Key Laboratory of Loess and Quaternary Geology, Institute of Earth Environment, Chinese Academy of Science, Xi'an, China
[g] Environment Research Institute, Shandong University, Qingdao, Shandong, China
[h] School of Water Conservancy and Environment, University of Jinan, Jinan, Shandong, China
[i] State Environmental Protection Key Laboratory of the Cause and Prevention of Urban Air Pollution Complex, Shanghai Academy of Environmental Science, Shanghai, China

HIGHLIGHTS

- Dust reverse-transport phenomena were used to study the aging process of dust plumes.
- East Asian dust plumes were prone to aging when transported to the south of Qingdao.
- Secondary sulfate/nitrate formation was strongly influenced by the precursors' concentrations on dust transport pathways.

ARTICLE INFO

Keywords:
Dust
Reverse-transport
Sulfate
Nitrate
Transport pathway
Secondary formation

ABSTRACT

Sulfate and nitrate formed on dust aerosols can considerably affect particles' physicochemical properties due to their high hygroscopicity. Dust reverse-transport (DRT) events can occur in eastern China when dust plumes undergo a distinct turn caused by Asian highs or cyclones, resulting in the re-appearance of the dust plume in one place but with anthropogenic pollutants mixed in. In this study, three DRT events were identified at a coastal city, Qingdao. The secondary sulfate and nitrate in $PM_{2.5}$ collected during the DRT events were estimated according to the mass concentration of water-soluble ions and dust tracer metal. Several key factors, including heterogeneous reactions on aerosols, photochemical conversions in the air, and precursors' abundance in dust plumes, affected the aging of dust plumes. In the presence of adequate ammonium and high-level oxidants in the air, sulfate and nitrate were efficiently produced under moderate/high humidity conditions when DRT events occurred to the south of Qingdao. The proportions of the secondary sulfate/nitrate in total concentrations exceeded 90%, in which 20.8%–43.1% of secondary nitrate was formed on dust particles. In contrast, when the DRT occurred to the north of Qingdao with low relative humidity and low $[NH_4^+]/[SO_4^{2-}]$ ratio, the growth of sulfate and nitrate was small. This study reveals a manner of efficient sulfate and nitrate formation in dust plumes in the continental atmosphere.

* Corresponding author. Frontier Science Center for Deep Ocean Multispheres and Earth System (FDOMES) and Physical Oceanography Laboratory, Ocean University of China, Qingdao, Shandong, China.
** Corresponding author. Frontier Science Center for Deep Ocean Multispheres and Earth System (FDOMES) and Physical Oceanography Laboratory, Ocean University of China, Qingdao, Shandong, China.
E-mail addresses: shenglf@ouc.edu.cn (L. Sheng), yangzhou@ouc.edu.cn (Y. Zhou).

https://doi.org/10.1016/j.atmosenv.2022.119518
Received 21 September 2022; Received in revised form 21 November 2022; Accepted 24 November 2022
Available online 29 November 2022

1. Introduction

East Asian deserts, such as the Gobi Desert and the Taklimakan Desert, are the main sources of global dust aerosols (Huang et al., 2014). Strong westerlies transport mineral dust emitted from the desert eastward, crossing areas with high urban density and intense human activity (Mahowald et al., 2005; Park et al., 2007; Zhang et al., 2010). When dust particles are mixed with anthropogenic pollutants or other types of aerosols, considerable amounts of secondary pollutants can form on the surface of dust particles under appropriate weather conditions (Li et al., 2014; Yuan et al., 2008). This phenomenon, known as dust aging, can change the morphology of dust particles and modify the radiative and hygroscopic properties of dust aerosols, and further influence their climate effects (Choobari et al., 2014; Huang et al., 2014; Li et al., 2014; Shi et al., 2008; Tang et al., 2016).

Dust aging has been studied intensively. Investigations on the mixing state and morphology of dust aerosols suggested that $CaSO_4$ and $Ca(NO_3)_2$ can be formed through heterogeneous reactions during dust transport (Dall'Osto et al., 2010; Li et al., 2014; Mori et al., 2003; Pan et al., 2017; Qi et al., 2018; Zhang and Iwasaka, 1999; Zhang et al., 2000, 2003), and the formation of sulfate and nitrate on the surface of dust particles can change its morphology to be more "rounded" (i.e., decrease the aspect ratio) (Pan et al., 2017). These studies used high-precision single particle detection instruments or electron microscopy. As aluminum is a typical tracer of mineral dust, the mass ratios of SO_4^{2-}/Al and NO_3^-/Al, the correlations between ions and Al, and the ratios of anthropogenic metals (e.g., Cu, Zn, Pb) to Al were used to reflect the mixing state of dust with anthropogenic pollutants in filter sampling studies (Sun et al., 2010; Takahashi et al., 2011; Wang et al., 2006, 2011, 2014a, 2016; Yuan et al., 2008; Zhang et al., 2010). In addition, mechanisms for the secondary formation of sulfate and nitrate have been studied in detail in laboratory experiments (He et al., 2014; Liu et al., 2012; Prince et al., 2007; Sullivan et al., 2009; Zhang et al., 2019b) and models (Cheng et al., 2016; Wang et al., 2017; Zhang et al., 2019a). Although aging processes have been commonly observed in the downstream area of dust transport, the determination of secondary pollutant formation remains a nontrivial task because dust plumes always carry some original pollutants (e.g., sulfate) emitted from desert areas (Tang et al., 2019; Wu et al., 2012), which may be mixed with other secondary formed materials.

The aging of dust plumes during long-distance transport has been observed for decades (Geng et al., 2014; Kim and Park, 2001; Mori et al., 2003), and researchers have found that the chemical composition could be influenced by the transport pathway, which was determined by atmospheric circulation (Onishi et al., 2012). However, the weather conditions that favor the generation of sulfate and nitrate in dust plumes, and the corresponding causes, remain ambiguous (Wu et al., 2017). In this paper, we studied three dust cases, during which the dust transport pathway changed significantly in eastern China. We named it dust-reverse transport (DRT). The DRT phenomenon is advantageous to the study of dust aging because it often leads to a long duration of dust weather in eastern China (Li et al., 2019). Previous studies show that it occurred 1–4 times annually during 2011–2018 (Li et al., 2019; Wang et al., 2017). A brief introduction of the DRT phenomenon can be found in Text S1 and Fig. S1 (supporting information).

Dust has a predominant number concentration in the fine mode, although its mass is distributed more in the coarse mode (Chun et al., 2001; Wang et al., 2018; Zhou et al., 2021). Fine mode particles ($PM_{2.5}$) are easier to transport over long distances and prone to aging than coarse particles (Wang et al., 2005). In another way, $PM_{2.5}$ usually contains much higher soluble iron, which is critical to regulating the marine ecological system (Gao et al., 2019; Xu and Gao, 2017), and the dissolution of iron is very closely related to the dust aging (Zhu et al., 2020). The present study focuses on secondary aerosol formation in $PM_{2.5}$. A modified method is explored to evaluate the formation of secondary sulfate and nitrate during the dust aging process, and the potential mechanisms are discussed. This study aims to determine the degree of aging of Asian dust plumes and the key factors influencing dust aging in eastern China.

2. Methodology and dataset

2.1. Sampling and chemical analysis

Aerosol sampling instruments were deployed at Baguanshan Atmospheric Research Observatory (BARO, 36°03′ N, 120°20′ E, about 76 m above sea level), which is located in the Shinan District, Qingdao. It is about 0.7 km away from the southern coastline (Fig. 1). The observation site is adjacent to the east edge of the North China Plain (NCP), and the Yellow Sea is to the east. It is a typical coastal site on the long-distance transport pathways of dust plumes from northern or northwestern China to the Yellow Sea.

Aerosol sampling was conducted from April 24 to May 27, 2017, March 28 to April 30, 2018, and May 22–28, 2018 (all dates and times refer to local time). The samples were collected separately during the daytime and nighttime (each sample lasted 10–13 h). Intensive sampling with higher temporal resolution (2.5–6 h) was implemented when dust events occurred. A total of 158 fine particle samples ($PM_{2.5}$) were collected by two high-volume $PM_{2.5}$ samplers (TISCH, TE-6070BLX-2.5, USA) at a flow of 1.06 m^3/min. During the campaign, two samplers ran simultaneously, one collecting fine particles on quartz microfiber filters (QM-A, PALL) and the other on Whatman® 41 filters. All QM-A filters had been heated at 450 °C for 6 h before sampling to remove background organic matter. Field blank samples were also collected at the beginning and end of the campaign. After sampling, QM-A filters and Whatman® 41 filters were sealed and stored at −20 °C until analysis.

QM-A filter samples were cut into pieces and extracted with 25 ml Milli-Q pure water in polyethylene tubes (WATSON) by ultrasonic vibration (0 °C) for 40 min. After that, the water extracts were filtered by syringes with 0.45 μm strainer heads (PALL). Then, water-soluble inorganic ions (WSIs, including K^+, Na^+, Mg^{2+}, Ca^{2+}, NH_4^+, F^-, Cl^-, SO_4^{2-}, NO_3^-) were analyzed by ion chromatography (IC, Dionex ICS-3000, Dionex Corp., Sunnyvale, CA, USA). The detection limit of these ions was about 10–40 μg L^{-1} and the uncertainty was 10%–15% of species' concentrations for our sampling frequency. Field blank membranes were also analyzed for correction. The charge balance of WSIs was analyzed to assure the reliability of the dataset. As shown in Fig. S2, the slope of the regression line of dust samples (k = 1.00) was lower than non-dust samples (k = 1.27). Because CO_3^{2-} cannot be measured by ion chromatography and dust particles usually contain CO_3^{2-} species, e.g., $CaCO_3$, the lower slope of the regression line indicates the influence of dust. In addition, the detection of elements is introduced in Text S2.

2.2. Air quality data, synoptic data and satellite data

Air quality data were obtained from the air quality monitoring network developed by the Ministry of Ecological Environment of the People's Republic of China (http://www.mee.gov.cn/). The network consists of more than 1600 ground stations (Fig. S3), and the west substation in the Shinan District of Qingdao is about 5.0 km away from the sampling site (the yellow dot in Fig. 1). The dataset includes hourly mass concentrations of $PM_{2.5}$, PM_{10}, SO_2, NO_2, O_3 and CO.

The regional synoptic situation during dust transport was studied using the ERA5 reanalysis data provided by the European Centre for Medium-Range Weather Forecasts (ECMWF) (https://cds.climate.copernicus.eu/cdsapp#!/search), with 0.25° × 0.25° and 6 h resolution. Weather conditions at the sampling site were analyzed using the data provided by the Qingdao Meteorological Station (about 1.1 km west of the sampling site) with a time resolution of 10 min. The temporal and spatial distributions of dust air masses were monitored using CALIOP cloud/aerosol profile data products (https://www-calipso.larc.nasa.gov/).

2.3. Determination of dust transport pathways and the concentrations of pollutant gases during dust transport

The HYbrid Single-particle Lagrangian Integrated Trajectory (HYSPLIT) Model (https://www.ready.noaa.gov/HYSPLIT.php) was utilized to investigate the transport of dust plumes (Zhou et al., 2015). It has been developed by the National Oceanic and Atmospheric Administration (NOAA) to study the transmission of air masses and the diffusion and deposition of atmospheric particles (Stein et al., 2015). The gridded (0.5° × 0.5° horizontal resolution) meteorological analysis data provided by the National Center for Environmental Prediction (NCEP) was used as the input data.

The chemical composition of dust particles may be modified by the precursors of secondary pollutants during dust transport. Thus, the HYSPLIT model was also used to estimate the concentrations of pollutant gases (i.e., SO_2, NO_2, CO, O_3) near the ground along the dust transport pathway. The average concentrations (C_i) of pollutant gases, for areas the dust plumes passed over during the 48 h before the arrival at the monitoring site, were calculated as follows,

$$C_i = \overline{\sum_{j=1}^{m} \sum_{n=1}^{48} C_{i,j,n}} \quad (1)$$

For sample i, at each hour j, 48 nodes (the time interval between two nodes is 1 h) on the transport pathway were selected based on backward trajectories (the ending height is 300 m). Herein m is the sampling duration of sample i, which means sample i has m trajectories. We calculated the average value of pollutant gases at each trajectory node $C_{i,j,n}$ by averaging the concentrations of the target pollutants at all air quality monitoring stations within a radius of 150 km with the trajectory node as the circle center (Fig. 2), and $C_{i,j,n}$ was used to estimate the polluted gas concentration of dust plumes passing this location.

Due to the limitation of the station distribution, some trajectory nodes have no air quality data. Most of these nodes are located in deserts or marine areas. The lack of data at those nodes was compensated in two ways. One is to eliminate these nodes and only calculate the nodes with polluted gas data, denoted as SO_2 (Partial) and NO_2 (Partial). The other is to set the polluted gas concentrations of these nodes to zero, denoted as SO_2 (All) and NO_2 (All). The results of these two methods actually exhibit a high degree of consistency (Fig. S4). So, the following discussion only involves the data sets of SO_2 (Partial) and NO_2 (Partial), named SO_2 (path) and NO_2 (path), to distinguish them from the local gas data. In addition, the DRT usually occurs in the lower troposphere (Li et al., 2019), for which we use ground-based data to evaluate the concentrations of pollutant gases in dust plumes during the DRT period.

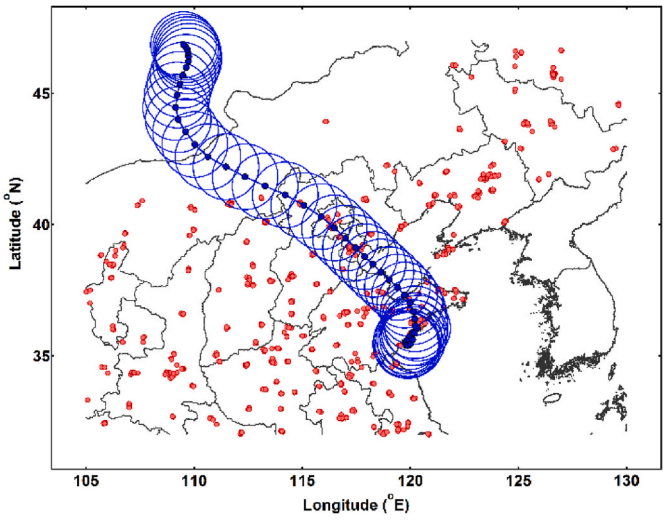

Fig. 2. Sketch map of the node data selection of an air trajectory. Red dots are the locations of air quality monitoring stations. Blue circles show the selection range centered on air trajectory nodes with a radius of 150 km. (For interpretation of the references to colour in this figure legend, the reader is referred to the Web version of this article.)

2.4. Estimation of secondary sulfate and nitrate and the portion of secondary nitrate formed on dust particles

A modified method to estimate secondary ions formation was applied based on Wang et al. (2014). Secondary SO_4^{2-} and NO_3^- were calculated by the following equations:

$$d(s,i) = C_s^i - C_1^{'} \times C_{Al}^i \quad (2)$$

$$C_1^{'} = \frac{C_s^{ref}}{C_{Al}^{ref}} \quad (3)$$

where C_s^i and C_s^{ref} are the total concentrations of SO_4^{2-} or NO_3^- of sample i and the reference sample, respectively; C_{Al}^i and C_{Al}^{ref} are the Al concentrations of sample i and the reference sample, respectively. The reference sample was selected as the sample with the lowest $C_1^{'}$, which is a constant. This method is referred to as the constant standard estimation (CSE) method in this study. Although the proportion of dust particles in aerosols drops rapidly during dust transport, the mass ratios of SO_4^{2-}/Al and NO_3^-/Al of dusty components generally change marginally (Shen et al., 2007; Wang et al., 2011). Moreover, Al is mainly contributed by

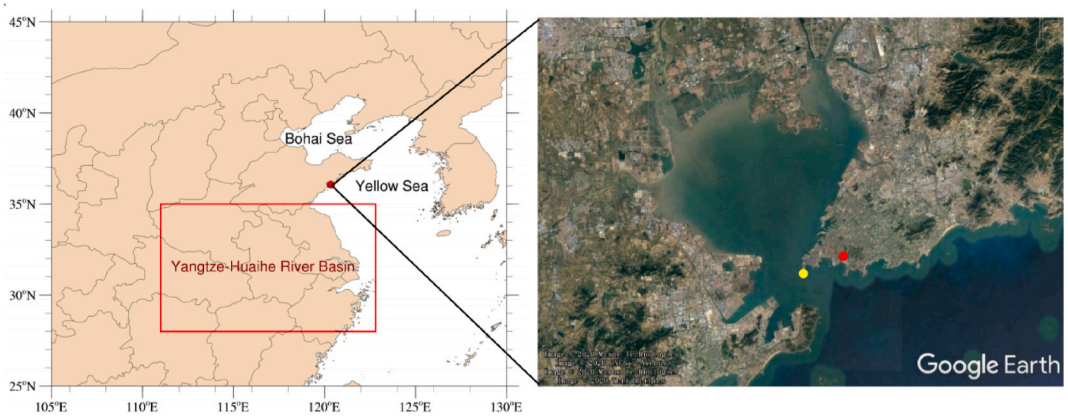

Fig. 1. Location of the sampling site. In the right panel, the red dot shows the location of the sampling site and the yellow dot shows the location of the air quality monitoring station (the west sub-station of the Shinan District) in Qingdao. The red rectangle in the left panel shows the domain of the Yangtze-Huaihe River Basin (YHRB). (For interpretation of the references to colour in this figure legend, the reader is referred to the Web version of this article.)

mineral dust in dust weather. Therefore, it is feasible to use $C_1^{'} \times C_{Al}^{i}$ to express the concentration of SO_4^{2-} and NO_3^- contributed by dust. And the secondary formed concentrations can be obtained from equation (2).

In addition, a chemical kinetic equation was utilized to differentiate secondary NO_3^- (calculated by the CSE method) that was formed on dust particles and isolated from dust particles. This method, labeled as chemical kinetic equation (CKE) method, utilizes the first-order chemical kinetic equation to estimate the uptake of HNO_3(g) during the transport, as shown by equations (4) and (5):

$$C_t = C_0 e^{-kt} \quad (4)$$

$$k = \frac{1}{4} v_{HNO3} \gamma_{HNO3} A_P \quad (5)$$

$$C_{on-dust} = C_t - C_0 \quad (6)$$

$$C_{isolated} = C_{secondary} - C_{on-dust} \quad (7)$$

where C_t is the concentration of HNO_3(g) at transport time t; C_0 is the initial mass concentration of HNO_3(g), which was evaluated by the ISORROPIA model (Text S4); k is the first-order rate at which the gaseous precursor is taken up by dust; v_{HNO3} is the mean molecular speed of HNO_3(g); γ_{HNO3} is the reactive uptake coefficient for HNO_3(g) on dust particles, and A_P is the total surface area of dust particles (Song et al., 2007). The portion of secondary NO_3^- formed on dust particles (named on-dust NO_3^-, i.e., equation (6)) was obtained by the difference between C_0 and C_t, and the remaining secondary NO_3^- was regarded as the one isolated from dust (named isolated NO_3^-, i.e., equation (7). If the calculated on-dust NO_3^- concentration was higher than the secondary NO_3^- estimated by the CSE method, we set that on-dust NO_3^- equals secondary NO_3^-. More details about the calculation by equations (4) and (5) can be found in Texts S3 and S4. While due to the tiny reactive uptake coefficient of SO_2, the on-dust SO_4^{2-} (average value is about 0.3 μg m^{-3} during dust cases) estimated by the CKE method was much lower than the observed SO_4^{2-}. Thus, the CKE method is inappropriate for simulating the complicated secondary processes of sulfate formation (Manktelow et al., 2010), and was not discussed in this study.

3. Dust transport and chemical composition variations during the DRT events

Ten dust cases occurred during the sampling period (Table S1). Three typical DRT events are studied in-depth in this paper (Fig. 3): Case 1 (May 5–8, 2017), Case 2 (May 12–14, 2017) and Case 3 (April 15–18, 2018). These cases are divided into two categories according to the synoptic conditions: the "south-high" DRT and the "moving-low" DRT (see details in Text S1). Case 1 and Case 3 were the same type of DRT event (south-high) that occurred in the Yangtze-Huaihe River Basin (YHRB, shown in Fig. 1), while Case 2 was a moving-low DRT event that occurred in the areas around the Bohai Sea (Fig. 1 and S1).

3.1. South-high DRT cases

In Case 1, the 48-h backward trajectory indicate that the dust plume moved southeastward from western Inner Mongolia (Fig. 4a). The dust arrived at the sampling site at about 1400 BST (Beijing standard time: GMT + 08:00; times below are all shown in BST) on May 5. The DRT of Case 1 occurred from May 6 to May 8 (Fig. 5). In Case 3, the dust plume was transported southward from the eastern Gobi area on April 14, 2018 (Fig. 4c). Invading dust arrived at Qingdao on April 15, passing over northern China and the Bohai Sea, and the DRT occurred in eastern China from April 16 to April 18 (Fig. 4c). The synoptic patterns of Case 1 and Case 3 during the DRT period are shown in Fig. S5a and S5c.

The mass concentrations of $PM_{2.5}$, PM_{10}, water-soluble ions in $PM_{2.5}$, and meteorological parameters during the three dust cases are summarized in Fig. 5. In Case 1, both $PM_{2.5}$ and PM_{10} increased sharply (Fig. 5c) and reached maximum levels of 161 μg m^{-3} and 892 μg m^{-3}, respectively, when the dust plume arrived at about 14:00 on May 5. Ca^{2+} can be used as a dust indicator, and its concentration and fraction in cations also increased significantly (Figs. 5d and S6a). The mass concentrations of sulfate, nitrate, and ammonium (SNA) in $PM_{2.5}$ increased from 0.51 μg m^{-3}, 0.15 μg m^{-3}, and 0.18 μg m^{-3} to 6.77 μg m^{-3}, 2.37 μg m^{-3}, and 0.53 μg m^{-3}, respectively, suggesting that the dust plume carried additional secondary pollutants (Fig. 5e). About 5 h after the dust arrival, the dust plume moved away, and the concentrations of PM dropped abruptly (Fig. 5c). During the DRT period (May 6–8), the concentrations of mineral components (e.g., Al, Ca) and SNA increased again. The SO_4^{2-} and NO_3^- concentrations on May 6 were comparable with those at the initial stage of Case 1, whereas they reached their

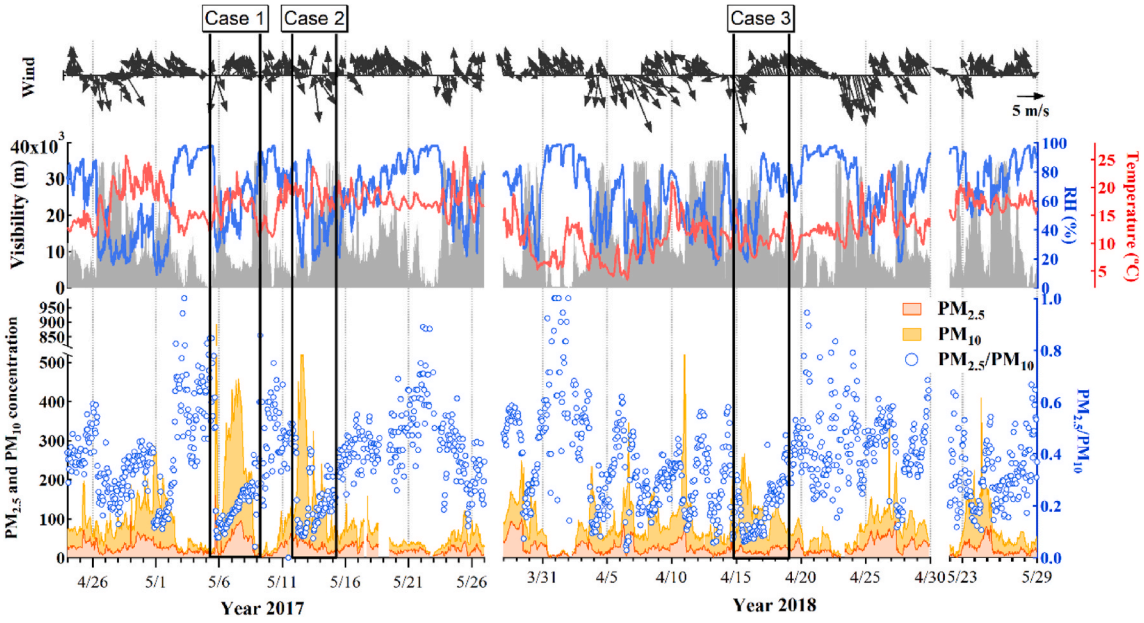

Fig. 3. Time series of meteorological parameters, atmospheric particle concentrations (unit: μg m^{-3}) and the mass ratio of $PM_{2.5}$ to PM_{10}.

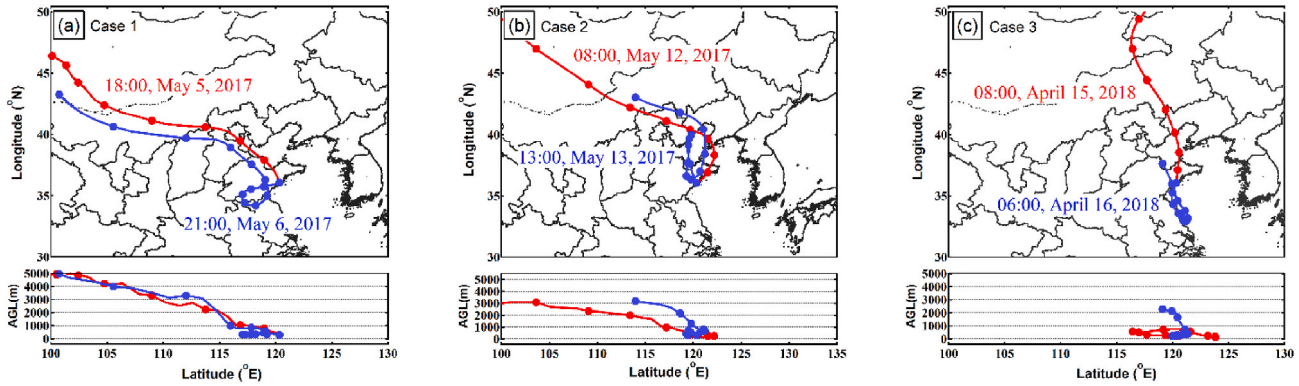

Fig. 4. Dust plume transport pathways (air mass backward trajectories for 48 h ending at a height of 300 m) and the corresponding height (above ground level, AGL) during the initial dust weather period (IDP, red) and the DRT period (blue). (For interpretation of the references to colour in this figure legend, the reader is referred to the Web version of this article.)

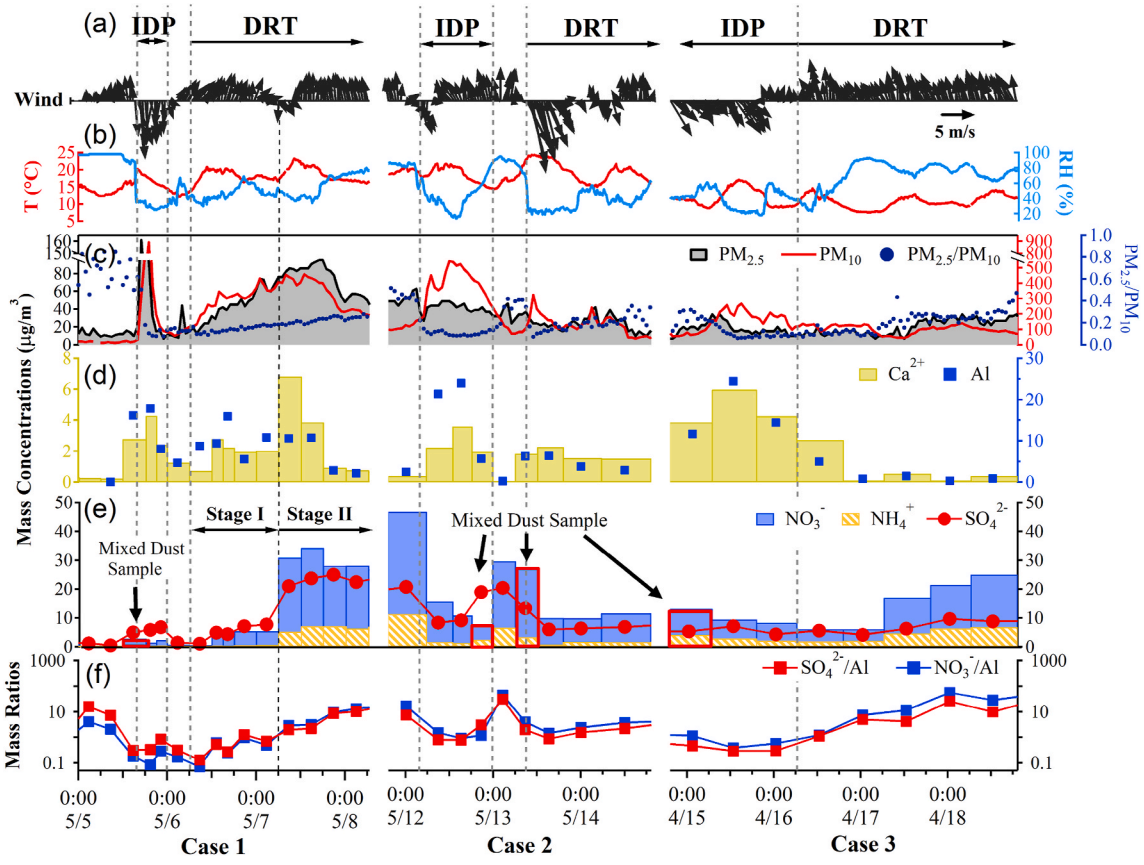

Fig. 5. Time series of (a and b) meteorological parameters, (c–e) mass concentrations of atmospheric particulates and several chemical species, and (f) mass ratios of SO_4^{2-}/Al and NO_3^-/Al during dust events. The initial stages and the DRT stages of the dust weather are illustrated as "IDP" and "DRT". Some mixed dust samples were specially marked by red frames in (e) according to the time series of meteorological parameters, air mass backward trajectories, and the mass ratio of $PM_{2.5}/PM_{10}$, which means there was a strong mix of dust and anthropogenic pollutants during the transition from non-dust period to dust period. (For interpretation of the references to colour in this figure legend, the reader is referred to the Web version of this article.)

maximum values on May 7 (Fig. 5e). The maximum concentrations of SO_4^{2-} and NO_3^- were 3.8 and 17.7 times their average values at the initial stage of Case 1, respectively, in 48 h after the DRT occurrence. Therefore, we divided the DRT period of Case 1 into two stages (stage I and stage II) according to the SNA concentrations (Fig. 5e). The average concentrations of SO_4^{2-} and NO_3^- at stage II were 3.6 times and 15.7 times higher than those at the first arrival of Case 1 (Table 1). We will discuss the formation of SO_4^{2-} and NO_3^- during these two stages in detail in Section 4.2.

During the dust aging process, secondary SO_4^{2-} and NO_3^- can form, while the mass concentration of Al may drop due to the deposition and dispersion of mineral dust. Therefore, the mass ratios of SO_4^{2-}/Al and NO_3^-/Al are usually used to estimate the degree of aging of dust plumes (Shen et al., 2007; Wang et al., 2006, 2011). They are usually less than 1 in fresh mineral dust (Table S2). The mass ratios of SO_4^{2-}/Al and NO_3^-/Al during the three dust cases of this study are shown in Fig. 5f and Table 1. In the initial stage of Case 1, the mass ratios of SO_4^{2-}/Al and NO_3^-/Al were 0.59 and 0.19, respectively, which were similar to the dust

Table 1
Summary of the mean concentrations of SO_4^{2-} and NO_3^- and mean values of mass ratios of SO_4^{2-}/Al and NO_3^-/Al during different stages in dust cases. Mixed dust samples were excluded.

	DRT type	Stage	SO_4^{2-} (μg m^{-3})	NO_3^- (μg m^{-3})	SO_4^{2-}/Al	NO_3^-/Al
Case 1	south-high	IDP	6.32	1.94	0.59	0.19
		Stage I of DRT	5.15	4.05	0.63	0.49
		Stage II of DRT	23.05	30.40	5.84	7.25
Case 2	moving-low	IDP	8.70	13.79	0.39	0.62
		DRT	6.50	10.72	1.83	3.03
Case 3	south-high	IDP	5.76	8.91	0.29	0.48
		DRT	6.88	15.23	8.88	20.58

particles collected in the locations near dust sources (Tazhong, Yulin and Horqin in Table S2), indicating fresh mineral dust. The mass ratios of SO_4^{2-}/Al and NO_3^-/Al increased gradually and reached a maximum of about 10 at the end of the DRT stage, apparently indicating the aging of the dust plume.

In Case 3, the air quality at Qingdao was not as good as that in Case 1 before the dust arrival. The mass concentration of SNA in $PM_{2.5}$ was much larger than in Case 1. The dust plume was transported to Qingdao on April 15 and the PM_{10} concentration reached its maximum of 267 μg m^{-3} (Fig. 5c). During the same period, the mass concentrations of NH_4^+ and NO_3^- in $PM_{2.5}$ decreased due to the dispersion by strong wind (Fig. 5e). However, there was no significant change in SO_4^{2-} concentration, probably due to the primary SO_4^{2-} in the dust plume or the secondary formation on dust particles. Dust sources may make a considerable contribution to SO_4^{2-} originating from a large number of salt lakes in the dust source region of Inner Mongolia, which contain sulfate minerals such as mirabilite (Tang et al., 2019; Williams, 1991; Zheng, 1991). The mass ratios of SO_4^{2-}/Al (0.29) and NO_3^-/Al (0.39) reached their lowest values in the initial stage (April 15) of Case 3 (Fig. 5f), which were comparable to the samples collected near dust sources, indicating relatively fresh dust plumes. In addition, there could be a potent mix of local anthropogenic emissions with the dust plume (marked as mixed dust sample in Fig. 5e) during the invasion of dust or when the dust plume was transported back to the sampling site, misleading the data analysis. Thus, in the following discussion, we excluded these mixed dust samples from the DRT samples.

On April 16, the DRT occurred and CALIPSO observations suggested the existence of dust aerosols in the near-ground atmosphere (Fig. S7), even though mineral components concentrations were low (Fig. 5d). The maximum concentrations of SO_4^{2-} and NO_3^- were 1.7 and 2.8 times as high as the average values at the initial stage, respectively, in 48 h since the DRT occurrence. The average values of SO_4^{2-} and NO_3^- during the DRT period were 1.2 and 1.7 times those at the initial stage (Table 1). Similar to Case 1, SO_4^{2-}/Al and NO_3^-/Al increased notably during the DRT period (Fig. 5f). The mass ratios of SO_4^{2-}/Al and NO_3^-/Al reached 5.02 and 7.44 on the night of April 16, respectively, indicating pronounced aging of the dust plume.

3.2. The moving-low DRT case

Backward trajectories show that the dust plume in Case 2 originated from the southeastern Gobi area (Fig. 4b). The PM_{10} geographical distribution and satellite observations (not given in this study) reveal that the dust plume moved southeastward in the afternoon on May 11, 2017, and passed over northern China, the Bohai Sea and the North Yellow Sea (Li et al., 2019). On the morning of May 12, Qingdao was affected by the dust plume. Although the wind direction (southeast/south wind) had changed during the daytime on May 12, Qingdao was still within the dust plume (Fig. 5a–d). In contrast to south-high DRT events, the air quality at the sampling site in Case 2 was poor before the arrival of the dust plume. The lowest $PM_{2.5}$ and PM_{10} concentrations were 44 μg m^{-3} and 95 μg m^{-3}, respectively, and the concentrations of SNA were much higher than in Cases 1 and 3 (Fig. 5e). When the dust plume arrived at Qingdao on May 12, the concentration of PM_{10} reached a maximum of 544 μg m^{-3}, with maxima of Ca^{2+} (3.6 μg m^{-3}) and Al (24.0 μg m^{-3}). The concentrations of SNA decreased due to the dilution by the dust plume. However, the SNA concentrations were still significantly higher than in the early stage of Case 1 (Fig. 5e). The mass ratios of SO_4^{2-}/Al and NO_3^-/Al were 0.39 and 0.62 during the initial dust period (IDP), respectively (Fig. 5f and Table 1), suggesting the dust plume did not undergo significant aging.

From the night of May 12 to the early morning of May 13, the dust plume gradually moved away from Qingdao under the south wind, corresponding to the intermittent period of dust influence. On the morning of May 13, the wind direction reversed and the dust plume returned to Qingdao under the northerlies. As shown in Fig. 5e, the last sample of the initial stage and the first sample in the DRT period with high SNA concentrations were also markered as mixed dust samples, during which Qingdao was affected by both dust and local sources (Fig. S8). The total concentrations of SO_4^{2-} and NO_3^- during the moving-low DRT period were similar to or even lower than the IDP period (Table 1). But, the proportion of NH_4^+ in cations increased gradually and reached more than 50% at the end, and NO_3^- accounted for more than 50% in anions (Fig. S6), indicating the formation of NH_4NO_3. The mass ratios of SO_4^{2-}/Al and NO_3^-/Al also increased gradually (Fig. 5f), but the values and rates of change were much lower than in south-high DRT cases, indicating relatively slow aging of the dust plume.

4. Secondary formation of sulfate and nitrate and influencing factors during dust transport

4.1. Contributions of secondary sulfate and nitrate

We did statistics of SO_4^{2-} and NO_3^- concentrations during different episodes in Fig. 6. South-high DRT samples were compared with the IDP samples and non-dust samples whose air masses also originated from the south. Since the air mass from the YHRB region influenced the south-high DRT samples, the statistics of other non-dust samples influenced by the south air mass ("south-airmass" samples) were also conducted. All dust events were considered in the statistics of the IDP samples. NO_3^- in both Case 1 and Case 3, and SO_4^{2-} in Case 1 showed significantly higher concentrations than the IDP samples, but comparable to or even lower than "south-airmass" samples. In this case, the DRT air mass might carry considerable local NO_3^- and SO_4^{2-} when it passed through the southern region. Thus, it is necessary to isolate the secondary ions formed on the dust from those in the anthropogenic plume.

Secondary NO_3^- and SO_4^{2-} were estimated by using the CSE method for these three DRT cases. Secondary NO_3^- was further classified into the mass formed on dust particles (on-dust NO_3^-) and isolated from dust (isolated NO_3^-) by the CKE method. On-dust NO_3^- might be underestimated because of the underestimation of A_p (Text S3). So, we can regard the on-dust NO_3^- estimated by the CKE method as the minimum value. As shown in Fig. 7a, the fractions of secondary NO_3^- increased significantly during the DRT periods in Case 1 and Case 3. About 24 h after the DRT occurrence, the fraction of secondary NO_3^- in total NO_3^- exceeded 90%. Secondary SO_4^{2-} showed similar variations (Fig. 7b). In stage I and stage II of Case 1, on-dust NO_3^- contributed 43.1% and 33.7% to secondary NO_3^-, respectively (Table S3). The highest fraction of on-dust NO_3^- to secondary NO_3^- could reach 59.3% during the DRT period in Case 1. While, during Case 3 DRT period, the fraction of on-dust NO_3^- to secondary NO_3^- was only about 20.8% due to fewer dust particles in Case 3 (Table S3). However, as shown in Fig. S9, the on-dust NO_3^- in unit dust mass (0.39 μg $μg^{-1}$) during Case 3 DRT period was similar to or even higher than in Case 1 DRT period (0.02 μg $μg^{-1}$ in stage I and 0.35 μg $μg^{-1}$ in stage II), indicating that the air condition during Case 3 DRT period was also conducive to the secondary nitrate formation on dust

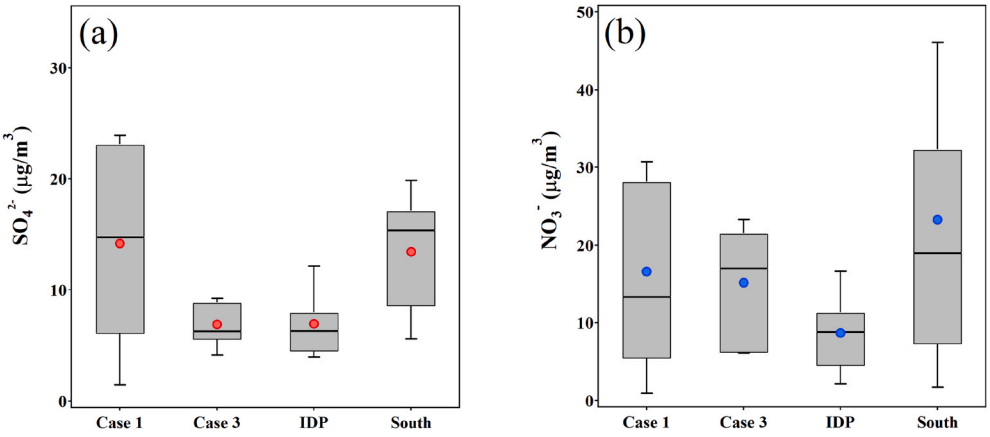

Fig. 6. Concentrations of (a) SO_4^{2-} and (b) NO_3^- during different episodes. Case 1 and Case 3 refer to their corresponding DRT samples. The IDP samples include the directly arrived dust plumes originated from northwest deserts. South samples were influenced by air mass from the south during the non-dust period, but the air mass originated from seas was excluded. Box and error bars represent the 25th, 50th 75th, 10th, and 90th percentiles, respectively, and red/blue dots illustrate the arithmetic mean. (For interpretation of the references to colour in this figure legend, the reader is referred to the Web version of this article.)

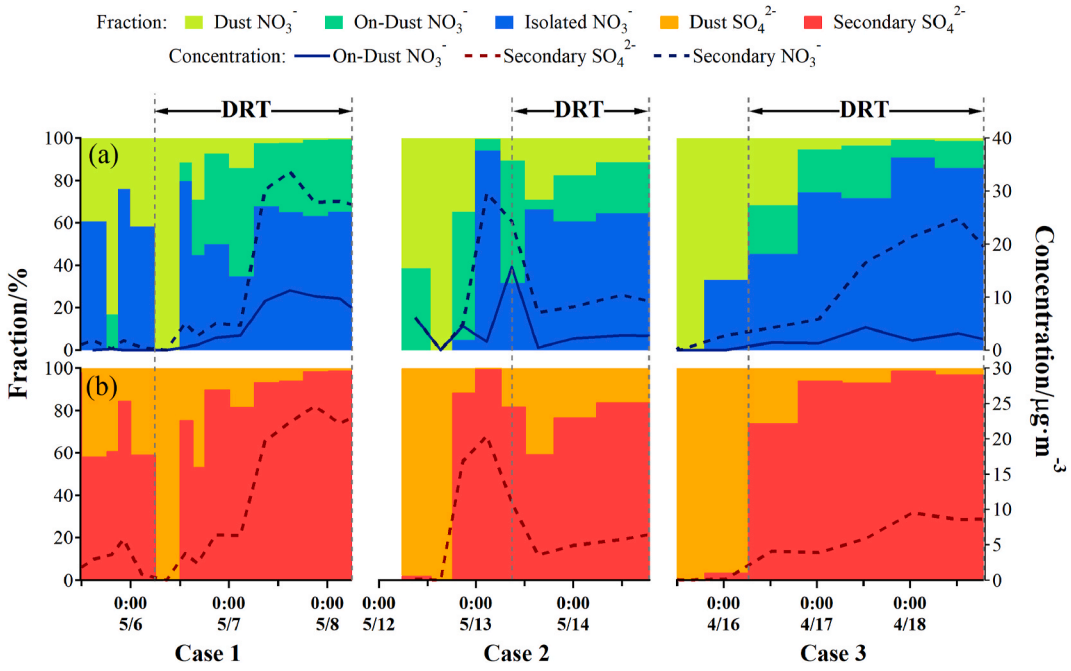

Fig. 7. Variations of the concentrations and fractions of NO_3^- (a) and SO_4^{2-} (b) from the dust source and the secondary formation. Secondary NO_3^- was divided into the NO_3^- formed on dust particles (on-dust NO_3^-) and the NO_3^- isolated from dust (isolated NO_3^-). The blue and red dotted lines represent the concentrations of secondary NO_3^- and secondary SO_4^{2-}, respectively. The solid blue line in (a) stands for the concentration of on-dust NO_3^-. (For interpretation of the references to colour in this figure legend, the reader is referred to the Web version of this article.)

surface. To investigate the roles that RH and temperature played in the formation of on-dust NO_3^-, we compared the dependence of the on-dust NO_3^- formation on the RH and temperature. Results showed that the influence of RH on the formation of on-dust NO_3^- was more significant than the temperature (Figs. S10, S11a and S12a). Both RH and temperature had minimal effects on HNO_3(g) concentration (Figs. S11b and S12b), but RH (related to γ_{HNO3}) had a more significant impact on the first-order rate of the chemical kinetic equation (i.e., k) than temperature (related to v_{HNO3}) (Figs. S11c and S12c). Therefore, the formation of on-dust NO_3^- is mainly controlled by RH when HNO_3 and the dust concentration are determined.

In the moving-low case (Case 2), apparent formation of the secondary SO_4^{2-} and NO_3^- were also identified during the DRT period, but the proportions of secondary SO_4^{2-} and NO_3^- in total concentrations were lower (80%–90% in the daytime on May 14) than those of the south-high DRT period (Fig. 7). The contribution of the dust plume to SO_4^{2-} and NO_3^- remained at about 10% 24 h after the DRT occurrence. On average, about 22.7% of the secondary NO_3^- would form on dust particles for the moving-low case (Table S3). However, on-dust NO_3^- in-unit dust mass was only about 0.14 μg μg^{-1} during the DRT period, much lower than in Case 1 and Case 3 (Fig. S9). The higher on-dust NO_3^- in-unit dust mass in the south-high DRT period indicated that secondary nitrate formation was more abundant than during the moving-low DRT period.

4.2. *Impact of precursors' concentrations and chemical reactions during dust transport*

Precursors' concentrations, ambient meteorology conditions and chemical reactions (e.g., heterogeneous reactions and photochemical processes) are essential factors influencing the secondary formation of SO_4^{2-} and NO_3^-. To explore the potential influence of precursors on the formation of secondary SO_4^{2-} and NO_3^- during the DRT events, we calculated the concentrations of SO_2 and NO_2 on the dust transport pathways by using the HYSPLIT model and precursors concentrations observed by ground stations on air mass transport pathways. As shown in Fig. 8b and 8d, SOR (the oxidation rate of sulfate, defined as $[SO_4^{2-}]$/

($[SO_4^{2-}]+[SO_2]$) and NOR (the oxidation rate of nitrate, defined as $[NO_3^-]/([NO_3^-]+[NO_2])$ varied similarly to their precursors. SOR, NOR, SO_4^{2-} and NO_3^- showed significant positive correlations with the SO_2 and NO_2 measured on dust transport pathways (Table 2), i.e., SO_2 (path), NO_2 (path) (R = 0.41–0.78), rather than the local data, indicating the precursor concentration on dust transport pathways had a more significant effect on the formation of SO_4^{2-} and NO_3^-.

In this study, aerosol liquid water content (ALWC) was estimated by ISORROPIA (Text S4). A clear increasing SO_4^{2-} and NO_3^- trends with ALWC and O_x (= O_x + NO_2) were observed (Fig. S13). Moreover, SOR and NOR also elevated significantly with the increase of RH (>40%) and O_x (>55 ppb) (Fig. S14), indicating both heterogeneous reactions and photochemical processes had conspicuous impacts on the secondary formation of SO_4^{2-} and NO_3^-.

4.3. Impact of relative abundance of ammonium

As mentioned in Section 3.1, we divided the DRT period of Case 1 into two stages according to SNA concentrations: stage I (mainly on May 6) and stage II (mainly on May 7). As shown in Table 1, the concentrations of SO_4^{2-}, NO_3^- and NH_4^+ in stage II were 4.5, 7.5 and 13.2 times as high as those in stage I, respectively, even though the $PM_{2.5}$ concentration was lower. The meteorological parameters (i.e., air temperature and RH) in stage I were similar to those in stage II, as were the concentrations of the precursors (Fig. 8a–c). One distinct difference between stage I and stage II was the relative abundance of NH_4^+. The remarkable increase in NH_4^+ concentration changed the mole ratio of $[NH_4^+]/[SO_4^{2-}]$ from 0.47 to 0.77 in stage I to 1.34–1.61 in stage II (Fig. 8d). The mole ratio of $[NH_4^+]/[SO_4^{2-}]$ exceeding 1.5 was used as a metric for ammonia-rich (AR) conditions, which favors the secondary formation of NO_3^- (Ding et al., 2019; Griffith et al., 2015).

Table 2
Pearson correlation coefficients of SOR, NOR, SO_4^{2-}, NO_3^- with precursor gases on air mass transport pathways (path) and in Qingdao (local) during dust events (Cases 1–3, N = 36). Values exceeding 0.5 significance are in bold.

	SO_2 (path)	NO_2 (path)	SO_2 (local)	NO_2 (local)
SOR	**0.61**	0.49	−0.16	−0.49
NOR	**0.60**	**0.52**	0.17	−0.25
SO_4^{2-}	**0.78**	0.42	0.42	−0.09
NO_3^-	**0.58**	0.41	0.42	0.04

In Case 3, the whole period was under AR conditions and the molar ratio of $[NH_4^+]/[SO_4^{2-}]$ was much higher than in Case 1 (Fig. 8d). However, the concentrations of SO_4^{2-} and NO_3^- were lower than in Case 1 (Fig. 5e). The peak concentrations of SO_4^{2-} and NO_3^- during the DRT period of Case 3 were 40.6% and 73.1% of those in stage II of Case 1, which was likely related to the lower precursor. The mass concentrations of SO_2 and NO_2 in Qingdao during the DRT period of Case 3 were 70.5% and 91.2% of those during the DRT period of Case 1.

Case 2 was mainly in AP (ammonia-poor, i.e., $[NH_4^+]/[SO_4^{2-}]$ <1.5]) conditions (Fig. 8d). The secondary formation of SNA was weaker during the DRT period compared with south-high DRT cases (Fig. 7). The concentrations of precursors were lower in dust plumes during the transport (Fig. 8b), and the low RH during the DRT period was not conducive to heterogeneous reactions and liquid-phase oxidation processes, which may lead to the slow aging of dust plumes.

4.4. Impact of air mass history on dust aging

The degree of aging of dust plumes varies greatly due to the physical

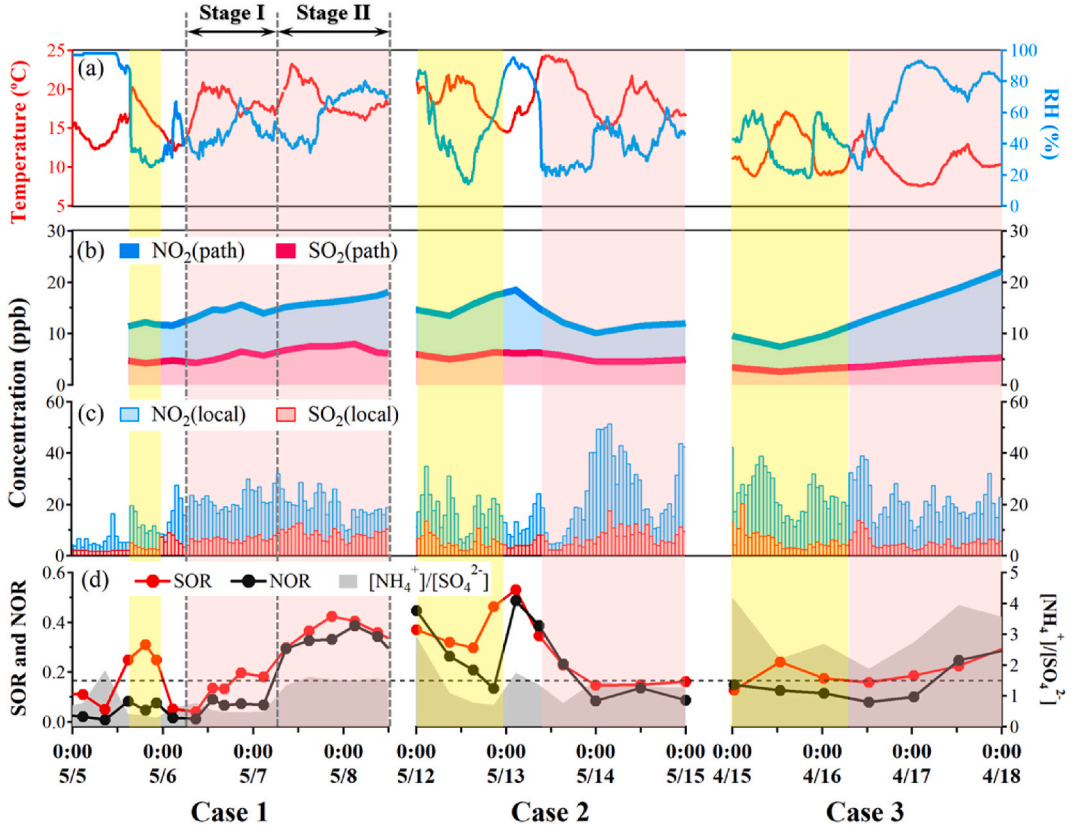

Fig. 8. Time series of (a) air temperature, relative humidity (RH), and average concentrations of SO_2 and NO_2 (b) on transport pathways of air masses and (c) in local Qingdao, respectively, and (d) chemical parameters of aerosols in Qingdao. Periods shaded yellow and red are the IDP and DRT periods of dust events, respectively. The dotted lines in (d) is a reference line with the molar ratio of $[NH_4^+]/[SO_4^{2-}]$ to 1.5. (For interpretation of the references to colour in this figure legend, the reader is referred to the Web version of this article.)

and chemical modifications between dust and local air pollutants when dust plumes pass through regions with different air pollution conditions. In this study, the Potential Source Contribution Function (PSCF, the details are introduced in Text S5) was used to explore the geographical distributions of potential SNA sources during the non-dust period to study the potential effect of dust transport pathways on dust aging. As shown in Fig. 9, the south of Shandong Province and the YHRB were the major contributors to high SNA concentrations. Extensive industrial activities in these areas result in high emissions of SO_2 and NO_x (Krotkov et al., 2016). The AR conditions (Fig. 9e) and high RH environment (Fig. S15) promote the formation of SNA in these areas. The dust plumes passing through these high pollutant areas aged rapidly in south-high DRT events (Case 1 and Case 3). In Case 2, the aged dust plume returned from the Bohai Sea, where less SO_4^{2-} and NO_3^- were expected and the aging of the dust plume was relatively slow. The YHRB also makes a large contribution to both SNA and anthropogenic trace metals (e.g., Hg, Cr, Cd, Pb, Ni) due to extensive industrial activities (Duan and Tan, 2013; Li et al., 2012; Tian et al., 2010, 2012a, 2012b, 2015). The heavy metals released by human activities can accumulate on the surface of dust particles, which may have a profound impact on the marine environment when transported eastward over the sea (Srinivas and Sarin, 2013).

5. Conclusions

In this study, the chemical characteristics and the aging process of dust plumes subject to the reverse-transport phenomenon (DRT) were studied. A modified method was applied to estimate the secondary formation of SO_4^{2-} and NO_3^-. Three dust cases with two different transport pathways showed very distinct aging processes. In south-high DRT cases, the transport direction of dust plumes was reversed by the high-pressure system in the Yangtze-Huaihe River Basin (YHRB, south of Qingdao). The concentrations of SO_4^{2-} and NO_3^- during the DRT period were 1.7–3.8 and 2.8–17.7 times their average values during the IDP period, and the contributions of secondary SO_4^{2-} and NO_3^- can reach more than 90%, respectively, within 24 h since the DRT occurrence. In contrast, the secondary formation of SO_4^{2-} and NO_3^- was much slower in the moving-low DRT case, when the DRT occurred near the Bohai Sea (north of Qingdao). The total concentrations of SO_4^{2-} and NO_3^- were at the same levels or even lower than those during the IDP period, and the dust source SO_4^{2-} and NO_3^- fractions remained about 10% 24 h after the DRT occurrence. Further study showed that 20.8%–43.1% of secondary NO_3^- was formed on the dust particles in south-high DRT cases and about 22.7% in the moving-low DRT case. In addition, the time series of SO_4^{2-} and NO_3^- were more consistent with the concentrations of SO_2 and NO_2 on dust transport pathways than those in the local area, indicating the significant influence of air mass history on dust aging. It was also verified that SNA formation was significant in AR conditions, in which heterogeneous and photochemical processes may play essential roles.

Our study highlighted the importance of dust transport pathways on dust aging. When dust plumes are transported to areas with abundant anthropogenic sources, polluted dust plumes may increase the solubility of heavy metals in dust particles, especially those emitted by human activities that become concentrated on dust aerosols. More soluble trace elements may significantly impact marine ecology when these dust particles are transported to the open ocean. A disadvantage of bulk sample analysis is that we cannot precisely figure out whether these secondary SNA were formed on dust particles or just due to the mixing of dust and local air pollutants during the transport of dust plumes. Thus, it is necessary to utilize multiple measurements, including the single-particle analysis, to have more accurate quantification in our future work.

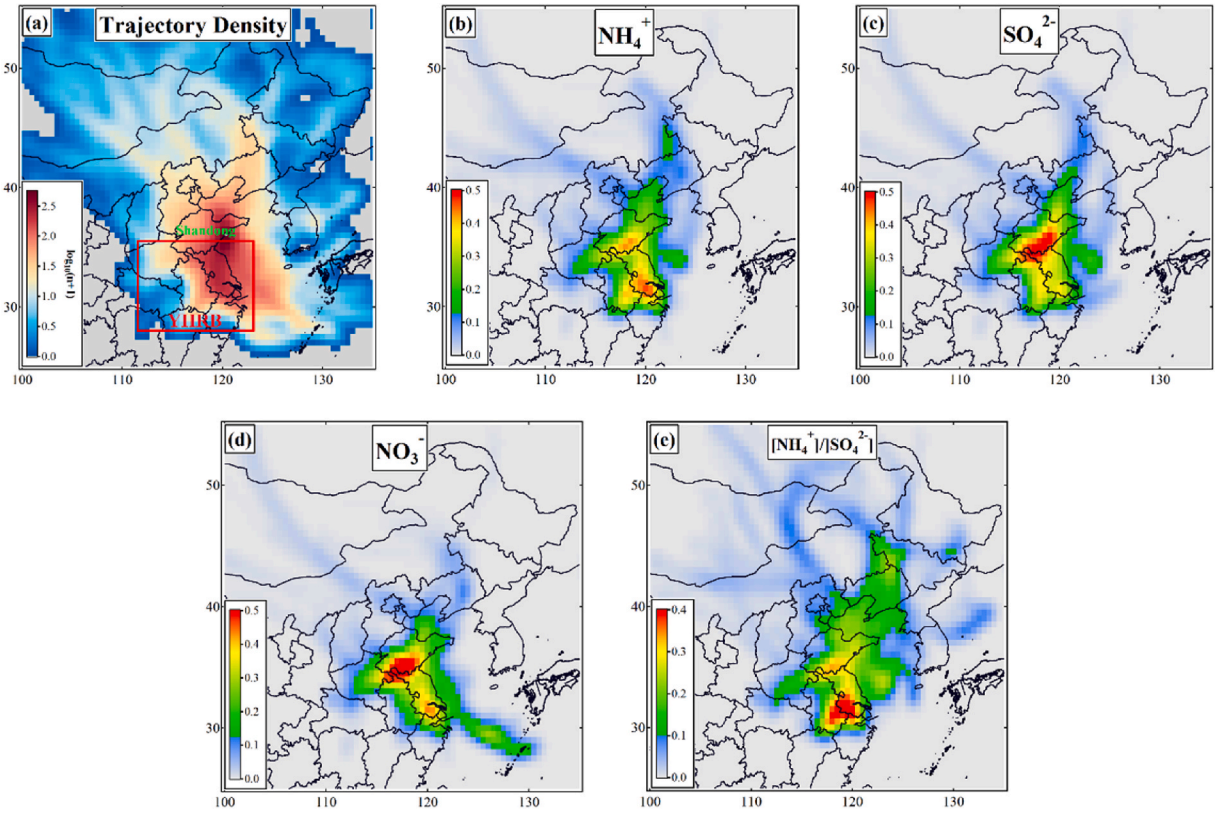

Fig. 9. PSCF results of (b) NH_4^+, (c) SO_4^{2-}, (d) NO_3^- and (e) $[NH_4^+]/[SO_4^{2-}]$ during the non-dust period. (a) shows the distribution of back-trajectory density during the non-dust period and the red frame represents the domain of the YHRB. Shandong Province is to the north of the YHRB. (For interpretation of the references to colour in this figure legend, the reader is referred to the Web version of this article.)

CRediT authorship contribution statement

Wenshuai Li: Methodology, Writing – original draft, Funding acquisition. **Yuxuan Qi:** Methodology, Data curation. **Wen Qu:** Methodology, Resources. **Wenjun Qu:** Methodology, Resources. **Jinhui Shi:** Methodology, Resources. **Daizhou Zhang:** Methodology, Writing – review & editing. **Yingchen Liu:** Methodology, Resources. **Feng Wu:** Methodology, Resources. **Yuanyuan Ma:** Methodology. **Yanjing Zhang:** Methodology. **Danyang Ren:** Methodology. **Xueqing Du:** Methodology. **Shishi Yang:** Methodology. **Xinfeng Wang:** Methodology, Resources. **Li Yi:** Methodology, Resources. **Xiaomei Gao:** Writing – review & editing. **Wencai Wang:** Methodology, Funding acquisition. **Yingge Ma:** Methodology, Resources. **Lifang Sheng:** Supervision, Writing – review & editing, Funding acquisition. **Yang Zhou:** Methodology, Supervision, Writing – review & editing, Project administration, Funding acquisition.

Declaration of competing interest

The authors declare that they have no known competing financial interests or personal relationships that could have appeared to influence the work reported in this paper.

Data availability

Data will be made available on request.

Acknowledgment

This research was supported by the National Natural Science Foundation of China (Grant Number: 41875155, 41605114, 41675146, 41875174), the Fundamental Research Funds for the Central Universities (Grant Number: 201961004) and the State Environmental Protection Key Laboratory of Formation and Prevention of Urban Air Pollution Complex. We are grateful to Shanhong Gao from the College of Oceanic and Atmospheric Sciences, Ocean University of China, for his support of our field campaign in Qingdao, China. We are grateful to Shaojie Song from the College of Environmental Science and Engineering, Nankai University, for his support with the ISORROPIA model calculation. The authors gratefully acknowledge the NOAA Air Resources Laboratory (ARL) for providing the HYSPLIT transport and dispersion model.

Appendix A. Supplementary data

Supplementary data to this article can be found online at https://doi.org/10.1016/j.atmosenv.2022.119518.

References

Cheng, Y.F., Zheng, G.J., Wei, C., Mu, Q., Zheng, B., Wang, Z.B., Gao, M., Zhang, Q., He, K.B., Carmichael, G., Poschl, U., Su, H., 2016. Reactive nitrogen chemistry in aerosol water as a source of sulfate during haze events in China. Sci. Adv. 2 (12), 11.

Choobari, O.A., Zawar–Reza, P., Sturman, A., 2014. The global distribution of mineral dust and its impacts on the climate system: a review. Atmos. Res. 138, 152–165.

Chun, Y., Kim, J., Cheon Choi, J., On Boo, K., Nam Oh, S., Lee, M., 2001. Characteristic number size distribution of aerosol during Asian dust period in Korea. Atmos. Environ. 35 (15), 2715–2721.

Dall'Osto, M., Harrison, R.M., Highwood, E.J., O'Dowd, C., Ceburnis, D., Querol, X., Achterberg, E.P., 2010. Variation of the mixing state of Saharan dust particles with atmospheric transport. Atmos. Environ. 44 (26), 3135–3146.

Ding, A.J., Huang, X., Nie, W., Chi, X.G., Xu, Z., Zheng, L.F., Xu, Z.N., Xie, Y.N., Qi, X.M., Shen, Y.C., Sun, P., Wang, J.P., Wang, L., Sun, J.N., Yang, X.Q., Qin, W., Zhang, X.Z., Cheng, W., Liu, W.J., Pan, L.B., Fu, C.B., 2019. Significant reduction of $PM_{2.5}$ in eastern China due to regional–scale emission control: evidence from SORPES in 2011–2018. Atmos. Chem. Phys. 19 (18), 11791–11801.

Duan, J., Tan, J., 2013. Atmospheric heavy metals and Arsenic in China: situation, sources and control policies. Atmos. Environ. 74, 93–101.

Gao, Y., Marsay, C.M., Yu, S., Fan, S., Mukherjee, P., Buck, C.S., Landing, W.M., 2019. Particle–Size variability of aerosol iron and impact on iron solubility and dry deposition fluxes to the Arctic ocean. Sci. Rep. 9 (1), 16653.

Geng, H., Hwang, H., Liu, X., Dong, S., Ro, C.U., 2014. Investigation of aged aerosols in size-resolved Asian dust storm particles transported from Beijing, China, to Incheon, Korea, using low–Z particle EPMA. Atmos. Chem. Phys. 14 (7), 3307–3323.

Griffith, S.M., Huang, X.H.H., Louie, P.K.K., Yu, J.Z., 2015. Characterizing the thermodynamic and chemical composition factors controlling $PM_{2.5}$ nitrate: insights gained from two years of online measurements in Hong Kong. Atmos. Environ. 122, 864–875.

He, H., Wang, Y., Ma, Q., Ma, J., Chu, B., Ji, D., Tang, G., Liu, C., Zhang, H., Hao, J., 2014. Mineral dust and NO_x promote the conversion of SO_2 to sulfate in heavy pollution days. Sci. Rep. 4 (1), 4172.

Huang, J., Wang, T., Wang, W., Li, Z., Yan, H., 2014. Climate effects of dust aerosols over East Asian arid and semiarid regions. J. Geophys. Res. Atmos. 119 (19), 11398–11416.

Kim, B.-G., Park, S.-U., 2001. Transport and evolution of a winter–time Yellow sand observed in Korea. Atmos. Environ. 35 (18), 3191–3201.

Krotkov, N.A., McLinden, C.A., Li, C., Lamsal, L.N., Celarier, E.A., Marchenko, S.V., Swartz, W.H., Bucsela, E.J., Joiner, J., Duncan, B.N., Boersma, K.F., Veefkind, J.P., Levelt, P.F., Fioletov, V.E., Dickerson, R.R., He, H., Lu, Z., Streets, D.G., 2016. Aura OMI observations of regional SO_2 and NO_2 pollution changes from 2005 to 2015. Atmos. Chem. Phys. 16 (7), 4605–4629.

Li, Q., Cheng, H., Zhou, T., Lin, C., Guo, S., 2012. The estimated atmospheric lead emissions in China, 1990–2009. Atmos. Environ. 60, 1–8.

Li, W., Wang, W., Zhou, Y., Ma, Y., Zhang, D., Sheng, L., 2019. Occurrence and reverse transport of severe dust storms associated with synoptic weather in east Asia. Atmosphere 10 (1).

Li, W., Shao, L., Shi, Z., Chen, J., Yang, L., Yuan, Q., Yan, C., Zhang, X., Wang, Y., Sun, J., Zhang, Y., Shen, X., Wang, Z., Wang, W., 2014. Mixing state and hygroscopicity of dust and haze particles before leaving Asian continent. J. Geophys. Res. Atmos. 119 (2), 1044–1059.

Liu, C., Ma, Q., Liu, Y., Ma, J., He, H., 2012. Synergistic reaction between SO_2 and NO_2 on mineral oxides: a potential formation pathway of sulfate aerosol. Phys. Chem. Chem. Phys. 14 (5), 1668–1676.

Mahowald, N.M., Baker, A.R., Bergametti, G., Brooks, N., Duce, R.A., Jickells, T.D., Kubilay, N., Prospero, J.M., Tegen, I., 2005. Atmospheric global dust cycle and iron inputs to the ocean. Global Biogeochem. Cycles 19 (4).

Manktelow, P.T., Carslaw, K.S., Mann, G.W., Spracklen, D.V., 2010. The impact of dust on sulfate aerosol, CN and CCN during an East Asian dust storm. Atmos. Chem. Phys. 10 (2), 365–382.

Mori, I., Nishikawa, M., Tanimura, T., Quan, H., 2003. Change in size distribution and chemical composition of kosa (Asian dust) aerosol during long–range transport. Atmos. Environ. 37 (30), 4253–4263.

Onishi, K., Kurosaki, Y., Otani, S., Yoshida, A., Sugimoto, N., Kurozawa, Y., 2012. Atmospheric transport route determines components of Asian dust and health effects in Japan. Atmos. Environ. 49, 94–102.

Pan, X., Uno, I., Wang, Z., Nishizawa, T., Sugimoto, N., Yamamoto, S., Kobayashi, H., Sun, Y., Fu, P., Tang, X., Wang, Z., 2017. Real–time observational evidence of changing Asian dust morphology with the mixing of heavy anthropogenic pollution. Sci. Rep. 7 (1), 335.

Park, S.S., Kim, Y.J., Cho, S.Y., Kim, S.J., 2007. Characterization of $PM_{2.5}$ aerosols dominated by local pollution and Asian dust observed at an urban site in Korea during Aerosol Characterization Experiments (ACE)–Asia Project. J. Air Waste Manag. Assoc. 57 (4), 434–443.

Prince, A.P., Kleiber, P., Grassian, V.H., Young, M.A., 2007. Heterogeneous interactions of calcite aerosol with sulfur dioxide and sulfur dioxide–nitric acid mixtures. Phys. Chem. Chem. Phys. 9 (26), 3432–3439.

Qi, J., Liu, X., Yao, X., Zhang, R., Chen, X., Lin, X., Gao, H., Liu, R., 2018. The concentration, source and deposition flux of ammonium and nitrate in atmospheric particles during dust events at a coastal site in northern China. Atmos. Chem. Phys. 18 (2), 571–586.

Shen, Z.X., Cao, J.J., Arimoto, R., Zhang, R.J., Jie, D.M., Liu, S.X., Zhu, C.S., 2007. Chemical composition and source characterization of spring aerosol over Horqin sand land in northeastern China. J. Geophys. Res. Atmos. 112 (D14).

Shi, Z., Zhang, D., Hayashi, M., Ogata, H., Ji, H., Fujiie, W., 2008. Influences of sulfate and nitrate on the hygroscopic behaviour of coarse dust particles. Atmos. Environ. 42 (4), 822–827.

Song, C.H., Kim, C.M., Lee, Y.J., Carmichael, G.R., Lee, B.K., Lee, D.S., 2007. An evaluation of reaction probabilities of sulfate and nitrate precursors onto East Asian dust particles. J. Geophys. Res. Atmos. 112 (D18).

Srinivas, B., Sarin, M.M., 2013. Atmospheric dry–deposition of mineral dust and anthropogenic trace metals to the Bay of Bengal. J. Mar. Syst. 126, 56–68.

Stein, A.F., Draxler, R.R., Rolph, G.D., Stunder, B.J.B., Cohen, M.D., Ngan, F., 2015. NOAA'S HYSPLIT atmospheric transport and dispersion modeling system. Bull. Am. Meteorol. Soc. 96 (12), 2059–2077.

Sullivan, R.C., Moore, M.J.K., Petters, M.D., Kreidenweis, S.M., Roberts, G.C., Prather, K. A., 2009. Timescale for hygroscopic conversion of calcite mineral particles through heterogeneous reaction with nitric acid. Phys. Chem. Chem. Phys. 11 (36), 7826–7837.

Sun, Y., Zhuang, G., Huang, K., Li, J., Wang, Q., Wang, Y., Lin, Y., Fu, J.S., Zhang, W., Tang, A., Zhao, X., 2010. Asian dust over northern China and its impact on the downstream aerosol chemistry in 2004. J. Geophys. Res. Atmos. 115 (D7).

Takahashi, Y., Higashi, M., Furukawa, T., Mitsunobu, S., 2011. Change of iron species and iron solubility in Asian dust during the long–range transport from western China to Japan. Atmos. Chem. Phys. 11 (21), 11237–11252.

Tang, M., Cziczo, D.J., Grassian, V.H., 2016. Interactions of water with mineral dust aerosol: water adsorption, hygroscopicity, cloud condensation, and ice nucleation. Chem. Rev. 116 (7), 4205–4259.

Tang, M., Zhang, H., Gu, W., Gao, J., Jian, X., Shi, G., Zhu, B., Xie, L., Guo, L., Gao, X., Wang, Z., Zhang, G., Wang, X., 2019. Hygroscopic properties of saline mineral dust from different regions in China: geographical variations, compositional dependence, and atmospheric implications. J. Geophys. Res. Atmos. 124 (20), 10844–10857.
Tian, H., Cheng, K., Wang, Y., Zhao, D., Lu, L., Jia, W., Hao, J., 2012a. Temporal and spatial variation characteristics of atmospheric emissions of Cd, Cr, and Pb from coal in China. Atmos. Environ. 50, 157–163.
Tian, H.Z., Wang, Y., Xue, Z.G., Cheng, K., Qu, Y.P., Chai, F.H., Hao, J.M., 2010. Trend and characteristics of atmospheric emissions of Hg, As, and Se from coal combustion in China, 1980–2007. Atmos. Chem. Phys. 10 (23), 11905–11919.
Tian, H.Z., Lu, L., Cheng, K., Hao, J.M., Zhao, D., Wang, Y., Jia, W.X., Qiu, P.P., 2012b. Anthropogenic atmospheric nickel emissions and its distribution characteristics in China. Sci. Total Environ. 417–418, 148–157.
Tian, H.Z., Zhu, C.Y., Gao, J.J., Cheng, K., Hao, J.M., Wang, K., Hua, S.B., Wang, Y., Zhou, J.R., 2015. Quantitative assessment of atmospheric emissions of toxic heavy metals from anthropogenic sources in China: historical trend, spatial distribution, uncertainties, and control policies. Atmos. Chem. Phys. 15 (17), 10127–10147.
Wang, G.H., Cheng, C.L., Huang, Y., Tao, J., Ren, Y.Q., Wu, F., Meng, J.J., Li, J.J., Cheng, Y.T., Cao, J.J., Liu, S.X., Zhang, T., Zhang, R., Chen, Y.B., 2014. Evolution of aerosol chemistry in Xi'an, inland China, during the dust storm period of 2013–Part 1: sources, chemical forms and formation mechanisms of nitrate and sulfate. Atmos. Chem. Phys. 14 (21), 11571–11585.
Wang, Q., Zhuang, G., Li, J., Huang, K., Zhang, R., Jiang, Y., Lin, Y., Fu, J.S., 2011. Mixing of dust with pollution on the transport path of Asian dust — revealed from the aerosol over Yulin, the north edge of Loess Plateau. Sci. Total Environ. 409 (3), 573–581.
Wang, Q.Z., Zhuang, G.S., Huang, K., Liu, T.N., Lin, Y.F., Deng, C.R., Fu, Q.Y., Fu, J.S., Chen, J.K., Zhang, W.J., Yiming, M., 2016. Evolution of particulate sulfate and nitrate along the Asian dust pathway: secondary transformation and primary pollutants via long–range transport. Atmos. Res. 169, 86–95.
Wang, X., Wen, H., Shi, J., Bi, J., Huang, Z., Zhang, B., Zhou, T., Fu, K., Chen, Q., Xin, J., 2018. Optical and microphysical properties of natural mineral dust and anthropogenic soil dust near dust source regions over northwestern China. Atmos. Chem. Phys. 18 (3), 2119–2138.
Wang, Y., Zhuang, G., Sun, Y., An, Z., 2005. Water–soluble part of the aerosol in the dust storm season—evidence of the mixing between mineral and pollution aerosols. Atmos. Environ. 39 (37), 7020–7029.
Wang, Y., Zhuang, G., Sun, Y., An, Z., 2006. The variation of characteristics and formation mechanisms of aerosols in dust, haze, and clear days in Beijing. Atmos. Environ. 40 (34), 6579–6591.
Wang, Z., Pan, X.L., Uno, I., Li, J., Wang, Z.F., Chen, X.S., Fu, P.Q., Yang, T., Kobayashi, H., Shimizu, A., Sugimoto, N., Yamamoto, S., 2017. Significant impacts of heterogeneous reactions on the chemical composition and mixing state of dust particles: a case study during dust events over northern China. Atmos. Environ. 159, 83–91.
Williams, W.D., 1991. Chinese and Mongolian saline lakes: a limnological overview. Hydrobiologia 210 (1), 39–66.
Wu, F., Zhang, D., Cao, J., Xu, H., An, Z., 2012. Soil–derived sulfate in atmospheric dust particles at Taklimakan desert. Geophys. Res. Lett. 39 (24).
Wu, F., Zhang, D., Cao, J., Guo, X., Xia, Y., Zhang, T., Lu, H., Cheng, Y., 2017. Limited production of sulfate and nitrate on front–associated dust storm particles moving from desert to distant populated areas in northwestern China. Atmos. Chem. Phys. 17 (23), 14473–14484.
Xu, G., Gao, Y., 2017. Characterization of atmospheric iron speciation and acid processing at metropolitan newark on the US east coast. Atmosphere 8 (4).
Yuan, H., Zhuang, G., Li, J., Wang, Z., Li, J., 2008. Mixing of mineral with pollution aerosols in dust season in Beijing: revealed by source apportionment study. Atmos. Environ. 42 (9), 2141–2157.
Zhang, D., Iwasaka, Y., 1999. Nitrate and sulfate in individual Asian dust–storm particles in Beijing, China in Spring of 1995 and 1996. Atmos. Environ. 33 (19), 3213–3223.
Zhang, D., Shi, G.-Y., Iwasaka, Y., Hu, M., 2000. Mixture of sulfate and nitrate in coastal atmospheric aerosols: individual particle studies in Qingdao (36°04′N, 120°21′E), China. Atmos. Environ. 34 (17), 2669–2679.
Zhang, D., Zang, J., Shi, G., Iwasaka, Y., Matsuki, A., Trochkine, D., 2003. Mixture state of individual Asian dust particles at a coastal site of Qingdao, China. Atmos. Environ. 37 (28), 3895–3901.
Zhang, S., Xing, J., Sarwar, G., Ge, Y., He, H., Duan, F., Zhao, Y., He, K., Zhu, L., Chu, B., 2019a. Parameterization of heterogeneous reaction of SO_2 to sulfate on dust with coexistence of NH_3 and NO_2 under different humidity conditions. Atmos. Environ. 208, 133–140.
Zhang, W., Zhuang, G., Huang, K., Li, J., Zhang, R., Wang, Q., Sun, Y., Fu, J.S., Chen, Y., Xu, D., Wang, W., 2010. Mixing and transformation of Asian dust with pollution in the two dust storms over the northern China in 2006. Atmos. Environ. 44 (28), 3394–3403.
Zhang, Y., Bao, F., Li, M., Chen, C., Zhao, J., 2019b. Nitrate–enhanced oxidation of SO_2 on mineral dust: a vital role of a proton. Environ. Sci. Technol. 53 (17), 10139–10145.
Zheng, X., 1991. Salt lakes on the inner Mongolian plateau of China. Chin. Geogr. Sci. 1 (1), 83–94.
Zhou, C., Zhang, X., Zhang, J., Zhang, X., 2021. Representations of dynamics size distributions of mineral dust over East Asia by a regional sand and dust storm model. Atmos. Res. 250, 105403.
Zhou, Y., Huang, X.H., Bian, Q., Griffith, S.M., Louie, P.K.K., Yu, J.Z., 2015. Sources and atmospheric processes impacting oxalate at a suburban coastal site in Hong Kong: insights inferred from 1 year hourly measurements. J. Geophys. Res. Atmos. 120 (18), 9772–9788.
Zhu, Y., Li, W., Lin, Q., Yuan, Q., Liu, L., Zhang, J., Zhang, Y., Shao, L., Niu, H., Yang, S., Shi, Z., 2020. Iron solubility in fine particles associated with secondary acidic aerosols in east China. Environ. Pollut. 264, 114769.